processes

MDPI

Article

Insights of Density Functional Theory into JP-10 Tetrahydrodicyclopentadiene Fuel Properties

Dilip Rijal [1], Vladislav Vasilyev [2], Yunxia Yang [3] and Feng Wang [1,*]

[1] Department of Chemistry and Biotechnology, Swinburne University of Technology, Melbourne, VIC 3122, Australia; drijal@swin.edu.au
[2] National Computational Infrastructure, Australian National University, Canberra, ACT 0200, Australia; vvv900@nci.org.au
[3] CSIRO Energy, 71 Normanby Road, Clayton North, VIC 3168, Australia; yunxia.yang@csiro.au
* Correspondence: fwang@swin.edu.au

Abstract: This study aims to investigate the structural, spectroscopic, and electronic properties of the synthetic missile fuel exo- and endo-tetrahydrodicyclopentadiene (THDCPD, JP-10) using density functional theory (DFT). It is to understand the dominance of the liquid exo-isomer (96%) of the jet fuel from the subtle differences between the isomers. The present DFT calculations reveal that the exo-isomer is 15.51 kJ/mol more stable than the endo-isomer, attributed to the flipping of the triangular ΔC8-C10-C9 ring in its norbornane skeleton. Calculated nuclear magnetic resonance (^{13}C-NMR) and infrared (IR) spectra, validated by experimental data, reveal larger chemical shifts for junction carbons (C1/C2 and C3/C4) due to reduced electron shielding and show distinct vibrational patterns. Charge analysis indicates that all carbon atoms are negatively charged except for the C1/C2 carbons which are positively charged in both isomers. While overall IR spectra of the isomers appear similar, bands near 3000 cm^{-1} correspond to distinctly different vibrational modes. The exo-isomer's electronic structure features a more delocalized HOMO and a larger HOMO-LUMO gap (7.63 eV) than the endo-isomer (7.37 eV). All such differences contribute to the properties of exo-THDCPD and, therefore, why the exo-isomer dominates JP-10 fuel.

Keywords: JP-10 aviation fuel; exo-/end-THDCPD; DFT calculations; NMR and IR spectroscopy

Academic Editor: Tanja Vidakovic-Koch

Received: 16 January 2025
Revised: 6 February 2025
Accepted: 11 February 2025
Published: 14 February 2025

Citation: Rijal, D.; Vasilyev, V.; Yang, Y.; Wang, F. Insights of Density Functional Theory into JP-10 Tetrahydrodicyclopentadiene Fuel Properties. *Processes* **2025**, *13*, 543. https://doi.org/10.3390/pr13020543

1. Introduction

High energy density (HED) fuels have gained considerable attention in the aerospace and defense sectors for their ability to deliver high-specific energy, making them essential for applications where weight is a critical constraint [1]. This advantage has spurred recent efforts to develop sustainable aviation fuels (SAFs) as researchers aim to create alternatives that are both efficient and sustainable [2–5]. The emphasis on HED fuels complements the growing demands for SAFs, which, under current standards of the American Society for Testing and Materials (ASTM International), can be blended with conventional jet fuels at up to 50% [3]. This blend compatibility highlights the role of SAFs in reducing aviation's environmental footprint while meeting the performance demands of high-energy applications. The possibility of transitioning to 100% SAFs is being explored to further reduce aviation's environmental footprint. For example, the emission and climate impact of alternative fuels (ECLIF3) study on commercial aircraft, such as Airbus A350, demonstrated that using 100% SAF substantially reduced 56% soot particle emissions and contrail formation compared to conventional fuels such as JetA-1 fuel [6]. Model

simulations projected that contrail-related climate impacts estimated a 26% reduction with 100% SAF [6].

Aviation fuels contain energy in the form of chemical potential energy stored within their molecular structures. This energy is primarily released through combustion or decomposition processes, such as in propulsion systems for rockets or advanced aircraft. Hydrocarbon fuels store energy within the chemical bonds such as C-H and carbon bonds to allow efficient oxidation during combustion, releasing significant heat [2,5,7]. A recent study found that many potential HED hydrocarbon fuel structures contain high H/C ratios and multiple rings [5]. Prominent examples of HED fuels include RJ-4, RJ-5, JP-10, T-10, and RJ-7 [1,2]. Among these, JP-10, also known as exo-tetrahydrodicyclopentadiene (exo-THDCPD, tricyclo [5.2.1.$0^{2,6}$]decane, CAS No. 2825-82-3, see Figure 1), stands out as a single-component fuel due to its exceptional physicochemical properties. With a high energy density of 39.6 MJ/L, excellent thermal stability, cost-effectiveness, and low freezing point [8,9], JP-10 is an ideal fuel for detailed studies.

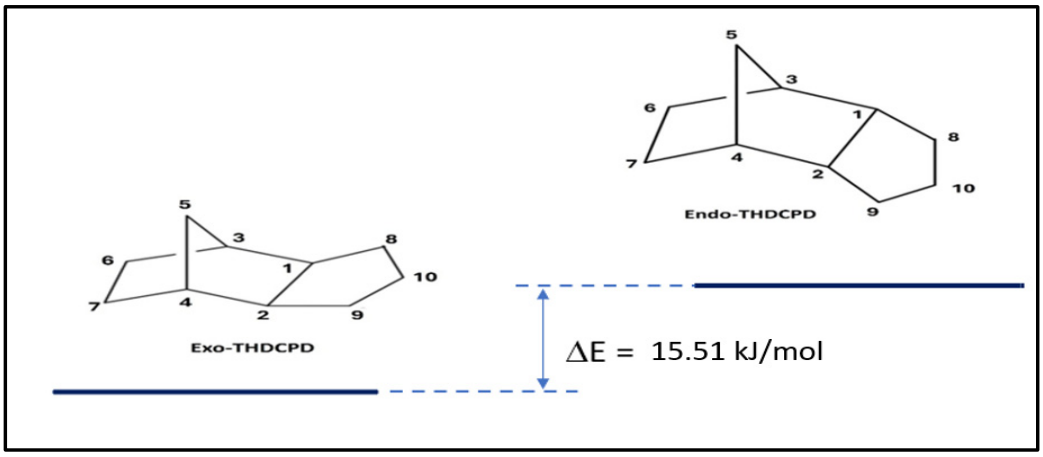

Figure 1. The chemical structures and nomenclature of endo- and exo-THDCPD (JP-10) isomers. The energy gap is based on the DFT B3LYP/aug-cc-pVTZ method of −390.830751 E_h for endo-THDCPD and −390.836484 E_h for exo-THDCPD, where the energy is the total electronic energy, including zero-point energy (ZPE).

Despite its widespread use, the rational design of next-generation HED fuels remains a significant challenge, largely due to the staggering number of potential candidates. For example, liquid hydrocarbons in the C5-C20 range amount to an estimated 2.7 million possible compounds, which include approximately 370,000 alkane isomers alone [10]. This immense chemical space makes experimental exploration infeasible, necessitating the use of advanced computational approaches. Machine learning (ML), combined with quantum mechanical insights, offers a powerful framework to address this complexity by enabling the rapid screening of vast molecular libraries and identifying optimal fuel candidates with targeted properties [2]. Such an integrated approach not only accelerates the discovery process but also enhances the understanding of the quantitative structure–property relationships (QSPRs) in the development of HED fuels. This paves the way for the rational design of next-generation fuels with improved performance and sustainability.

To effectively leverage ML in the rational design of HED fuels, it is essential to establish accurate databases and QSPRs. QSPR is fundamental to understanding how molecular structure governs key properties, such as energy, thermal stability, and volatility. Quantum mechanical methods, particularly density functional theory (DFT), play a pivotal role in this endeavor, providing accurate insights into the electronic structure, thermodynamics, and spectroscopic characteristics of compounds like JP-10. In addition, DFT calculations not only uncover the underlying structure–property relationships [11] but also serve as

benchmarks for validating and refining ML-generated descriptors. By integrating these quantum mechanical insights with ML, it becomes possible to develop QSPR descriptors that capture the nuanced features of molecular systems, enabling reliable predictions of properties for HED fuel candidates. This approach significantly enhances the efficiency of screening the vast chemical space of potential HED fuels, accelerating the discovery of novel compounds optimized for performance, safety, and sustainability.

Developing robust QSPRs requires high-quality data from well-characterized fuels, and JP-10 is an ideal candidate for such studies. As a single-component HED fuel, JP-10 offers a unique advantage with its well-documented physicochemical properties and relatively simple composition, making it easier to model compared to multi-component fuels. These attributes position JP-10 as a cornerstone for understanding and designing the next generation of HED fuels. In addition, ongoing research is focused on developing SAFs derived from strained hydrocarbons like exo-THDCPD, cis/trans-decalin, and norbornadiene [12]. These molecules hold the potential to enhance the volumetric energy content of conventional aviation fuels, such as Jet-A [13]. However, any new synthetic fuel formulations must adhere to ASTM D7566/D4054 standards [14,15] to ensure their physicochemical properties remain within regulated limits, a crucial requirement for ensuring both safety and efficiency in aviation performance. This work underscores the potential of HED hydrocarbons for high-energy applications and their role in advancing sustainable fuel solutions for aviation.

This study investigates the structural differences between the endo- and exo-isomers of JP-10 and their impact on HED characteristics. Using high-level DFT calculations, we are able to analyze variations in energy, freezing points, and thermal stability by examining electronic structures. While prior studies have explored JP-10 properties, a comprehensive experiment validated DFT analysis of endo-/exo-THDCPD isomers remains unexplored [11,16]. In addition to spectroscopic characterization, we computed electronic properties, including the HOMO-LUMO gap and valence orbitals, via the excess orbital energy spectrum (EOES) approach [17]. This work enhances understanding of the exo-THDCPD structure's role in JP-10's performance as a high-energy-density fuel. This article is organized as follows: Section 2 briefly describes the materials and methods, including the computational framework and spectroscopic techniques. Section 3 presents the results and discussion, highlighting the structural, electronic, and spectroscopic differences between the isomers. Finally, the key conclusions and proposed directions for future research are summarized in Section 4.

2. Methods

The primary source of endo-THDCPD can be synthesized from dicyclopentadiene (DCPD) through a hydrogenation process [18]. JP-10 (exo-THDCPD isomer) was predominantly generated by isomerizing its endo-THDCPD isomer in the presence of a powerful catalyst [18]. A key distinction between the HED fuel JP-10 and other conventional aviation fuels, such as Jet-A, is that JP-10 is considered a single-component fuel. It consists predominantly of exo-THDCPD (96.5%), with minor components including endo-THDCPD (2.5%) and adamantane (1%) [9]. The high purity of exo-THDCPD in JP-10 simplifies its study and optimization compared to the complex hydrocarbon mixtures in Jet-A fuel, offering a unique opportunity for detailed structural and performance analysis.

Despite their structural similarities, the two forms of THDCPD—endo- and exo-THDCPD—display markedly different physicochemical properties. For example, exo-THDCPD remains liquid even at very low temperatures, with a freezing point of −79 °C, while endo-THDCPD is solid under standard conditions, solidifying at 77 °C [19]. These significant differences in freezing points, along with the fact that exo-THDCPD is used as a

fuel and endo-THDCPD is not, highlight the importance of understanding the underlying factors that govern these properties.

The DFT computational details are as follows. The molecular structures of exo- and endo-THDCPD (refer to Figure 1) were optimized using DFT with the B3LYP and B3PW91 functionals and the aug-cc-pVTZ basis set, as implemented in the Gaussian 16 (Swinburne Supercomputing OzSTAR, Melbourne, VIC, Australia) software package [20]. Combining the DFT functionals with a large basis set such as aug-cc-pVTZ balances accuracy and computational efficiency [12,21–23], the aug-cc-pVTZ basis set (augmented correlation-consistent polarized valence triple-zeta) includes diffuse functions that capture long-range interaction [21], allowing a better prediction of internal structure. The absence of imaginary frequencies in the optimized structures confirms that both endo-THDCPD and exo-THDCPD are located at the energy minima, respectively, with stable configurations [12].

IR and NMR techniques are the most commonly used techniques to study fuels and composition [24–27]. Based on the optimized structures, IR, NMR, and EOES spectra were calculated using the same DFT methods as they are reliable with spectroscopic accuracy [12,22,23]. For NMR calculations, the gauge-invariant atomic orbital (GIAO) method was employed [28] to calculate the chemical shielding σ of the sample (fuel); chemical shifts (δ) need to reference the chemical shieling of tetramethylsilane (TMS), which is built in the software. The build-in absolute shielding for TMS was σ_C (TMS) = 182.47 ppm for ^{13}C and σ_H (TMS) = 31.88 ppm for ^{1}H, so that the chemical shifts (δ) of the sample (relative to TMS) is given by the following:

$$\delta_{sample} = \sigma(TMS) - \sigma_{sample} \quad (1)$$

Equation (1) is used for both ^{13}C and ^{1}H NMR chemical shifts, respectively. GaussView 6.0.16 [29] was employed to assist with some visual analysis and results.

3. Results and Discussion

3.1. Geometries of Endo/Exo-THDCPD Isomers

As indicated in Figure 1, the exo-THDCPD isomer is slightly more stable than the endo-THDCPD isomer by 15.51 kJ/mol calculated using the DFT B3LYP/aug-cc-pVTZ model. This finding aligns with previous computational studies and calorimetric measurements, which also identify the exo-isomer as the more stable form [30]. The corresponding cartesian coordinates for these optimized structures are provided in Table S1 of the Supplementary Materials.

Geometric properties, including bond lengths, such as C-C and C-H bonds and their connections (bond angles and dihedral angles), play a crucial role in determining the net heat of combustion (NHOC) for hydrocarbon fuels [5,12]. The former (bond lengths) dominate the energy of a compound, and the latter (bond angles and dihedral angles) determine the orientation and strain energy of the compound. The cartesian coordinates for the optimized geometries of the endo/exo-THDCPD isomers using the DFT B3LYP/aug-cc-pVTZ and B3PW91/aug-cc-pVTZ models are given in Table S2 of the Supplementary Materials.

The subtle geometric differences between the optimized structures and the electrostatic potential (ESP) of the endo- and exo-THDCPD isomers are given in Figure 2. Most calculated bond lengths and angles agree well with available experimental data (See Table S2 of the Supplementary Materials). The 3D structures of endo- and exo-isomers apparently differ in their dihedral angle (∠C8-C1-C2-C4), which controls the rotation around the C1-C2 bond, determining the endo- and exp-THDCPD configurations. For instance, the dihedral angle (∠C8-C1-C2-C4) flips markedly from −126.12° in endo-THDCPD to 122.83° in exo-THDCPD, indicating the distinct configurations of the two isomers in 3D. The flag angle ∠C3-C5-C4, although distorted significantly from the ideal bond angle of 109.5° of

C-C sp^3 hybridization [31], experiences only minor isomeric changes. For example, the flag angle ∠C3-C5-C4 for the exo- and endo-isomers is calculated as 94.51° and 94.22°, respectively, which is in close agreement with the available experimentally measured value of 94.5° for the exo-isomer [9].

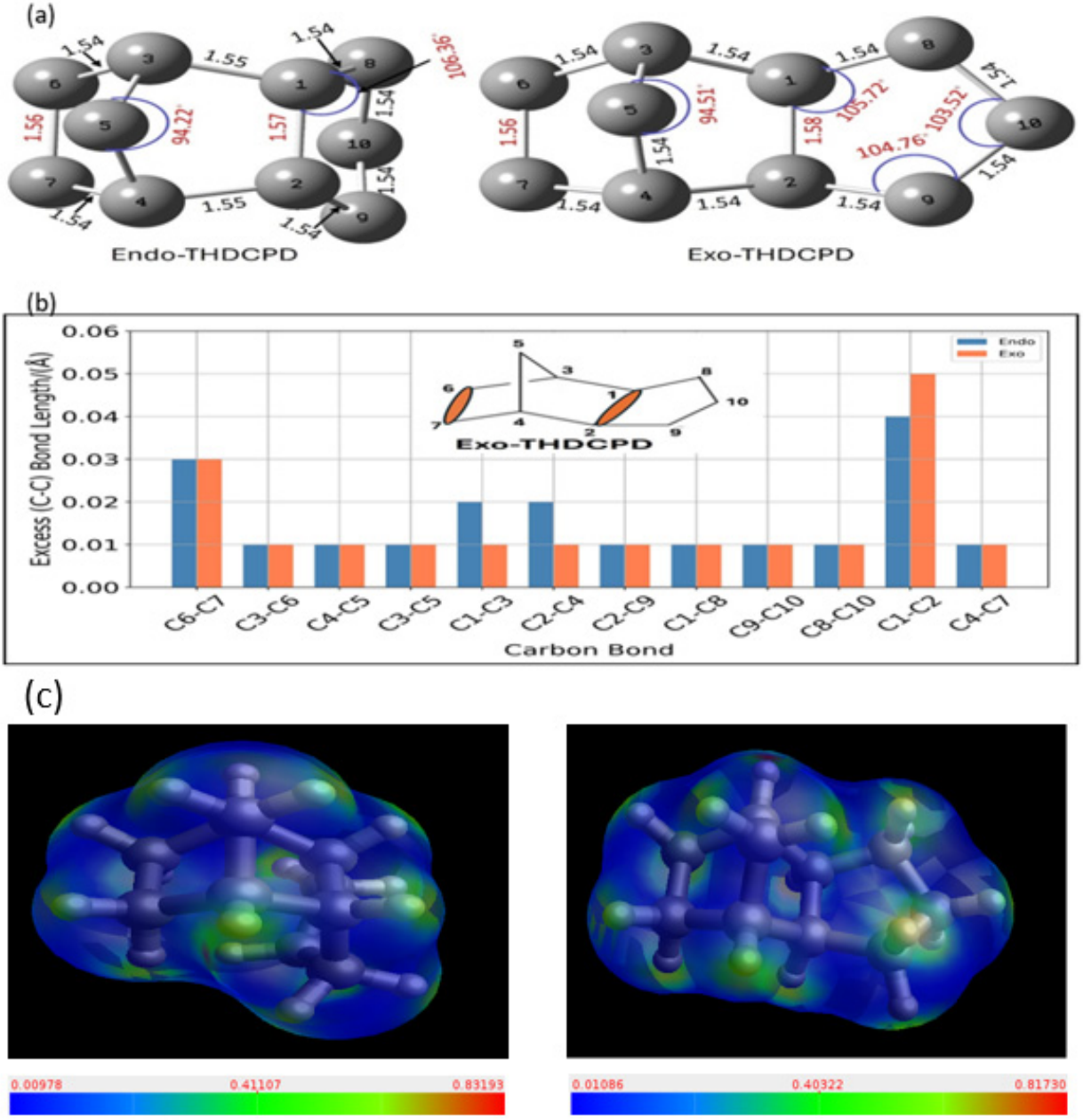

Figure 2. Optimized structure (**a**) of endo-THDCPD (left) and exo-THDCPD (right) using DFT B3LYP/aug-cc-pVTZ model. (**b**) The excess C-C bond lengths of endo- (blue) and exo-THDCPD (orange) with respect to C-C of Ethane (1.53 Å) using the same model (B3LYP/aug-cc-pVTZ), and (**c**) the calculated electrostatic potentials (ESP) of endo (left) and exo (right) isomers of THDCPD.

Figure 2 also reports that the cyclic structure and selected geometric parameters (bond angles and C–C bond lengths) distort more in endo-THDCPD compared to exo-THDCPD. For example, the C1-C3 and C2-C4 pair of bonds stretched more in endo-THDCPD, as shown in Figure 2b for the excess C-C bond lengths of endo/exo-THDCPD (JP-10) with respect to isolated C-C bonds in ethane, which observed as 1.54 Å experimentally [32]. All C-C bond lengths in THDCPD experience elongation of approximately 0.01 Å with respect to ethane. This may be due to the multicyclic carbon ring structure with secondary carbons

(CH_2) and tertiary carbons (CH) of the hydrocarbons with respect to primary carbons (-CH_3) in ethane. The most substantial deviation in C-C bond length of both isomers is the bridge tertiary C1-C2 bond with 0.04 Å and 0.05 Å, respectively, for endo- (1.57 Å) and exo-THDCPD (1.58 Å), as shown in Figure 2b. The tertiary bridge C1-C2 bond is shared by two rings, C1C2C7C6 and C1C2C9C10C8, in which the orientation of C1C2C9C10C8 ring may cause certain strain, particularly in the exo-isomer.

The next largely elongated C-C bond stretch is the terminal secondary C6-C7 bond, which extends approximately 0.03 Å for both endo-/exo-THDCPD isomers. It indicates that the orientation of the C1C2C9C10C8 ring in the isomers is too far to impact the C6-C7 bond. However, in the endo-THDCPD isomer, the bond lengths of tertiary C1-C3 and C2-C4 are larger, which suggests that the endo-THDCPD configuration impacts the C1-C3 and C2-C4 bond through space from the bottom, as shown in the optimized 3D structure in Figure 2a. Usually, in strained systems (like cyclopropane), C-C bonds are longer due to bond angle distortions, and these bonds are weaker, as bond length and bond strength are inversely correlated [33], potentially enhancing combustion efficiency. Table S2 in Supplementary Materials provides a detailed comparison of endo- and exo-THDCPD bond lengths, including available experimental data for exo-THDCPD.

The electrostatic potential (ESP) is crucial for understanding chemical reactivity and molecular structure in both molecules and solids. Various properties, such as atomic and anionic radii, electronegativities, and energies, can be derived from ESP calculations [34]. The ESP of the endo- (left) and exo- (right) isomers of THDCPD, obtained from DFT calculations, is shown in Figure 2c. These ESP values are computed at multiple points in space around the molecule [35]. Regions of positive electrostatic potential (blue) are depicted in Figure 2c.

Both isomers predominantly exhibit positive charge distributions. The endo isomer has a broader ESP range (0.00978 to 0.83193), indicating greater charge variation, while the exo isomer has a narrower range (0.01086 to 0.81730), suggesting a more uniform electrostatic surface that may enhance interactions with polar molecules or surfaces. The larger ESP variation in the endo isomer suggests greater electron density anisotropy, which could influence molecular packing and phase behavior. This may contribute to a higher freezing point and greater thermal stability, though these properties also depend on factors such as molecular packing, dipole interactions, and steric effects.

To further explore the structural distinctions between the THDCPD isomers, Table 1 compares some selected properties, such as dipole moment, polarizability, total electronic energy of the isomers, and electronic spatial extent $<R^2>$. It is not surprising that many isomers' properties can be very similar. However, for some isomers, such as THDCPD, small differences in their structures and properties may cause large differences in their functionalities. As a result, it is important to examine the small differences that may lead to a particular isomer's unique properties. The most obvious differences between the THDCPD isomers are their dipole moments, which are ten times smaller for exo-THDCPD (0.014 D) with respect to its endo-isomer (0.14 D), though the dipole moments are very small. Fuels with lower dipole moments generally exhibit reduced freezing points, a beneficial property for performance in cold environments [36]. Therefore, the low dipole moment of exo-THDCPD may enhance its suitability for aviation fuel, particularly in applications requiring resistance to freezing at low temperatures. The next apparent property difference is the electronic spatial extent $<R^2>$ [37]. This property of the endo-isomer is smaller than the exo-isomer by approximately 8%. Electronic spatial extent is a measure of the average spatial distribution of its electrons relative to the nucleus, and it provides insight into the spatial distribution of electrons and their overall "reach" within a molecule, reflecting the size, shape, and delocalization of the electron cloud. A larger value of $\langle R^2 \rangle$ in exo-THDCPD

suggests a more diffuse electron distribution, while endo-THDCPD with a smaller value indicates a more compact electron cloud and higher strain.

Table 1. Properties of endo- and exo-THDCPD isomers calculated using B3LYP/aug-cc-pVTZ *.

Properties	Endo-THDCPD	Exo-THDCPD
Dipole moment (μ) (Debye)	0.14	0.014
ETotal(Eh) #	−390.589648	−390.595828
Polarizability (α) (a.u)	108.12	109.56
$<R^2>$ (a.u)	1233.48	1344.41

* B3LYP/aug-cc-pVTZ models. The ΔE of 15.51 kJ/mol of exo-isomer is more stable than endo-isomer and is in good agreement with 12.7 kJ/mol calculated by Zehe and Jaffe [38] and 14 kJ/mol of Boyd et al. [39]. # The total electronic energy with the zero-point energy (ZPE).

3.2. Nuclear Magnetic Resonance (NMR) Chemical Shifts

Molecular spectroscopy is experimental quantum mechanics [40]. NMR techniques are the most commonly used techniques to study fuels and composition [24–27]. When combined with DFT-based calculations, complementary insights into their structure, properties, and local behaviors can be achieved [41–43]. The ^{13}C and ^{1}H-NMR chemical shifts in endo-THDCPD and exo-THDCPD are calculated in isolation as they minimize the intermolecular interactions. Table 2 compares the calculated ^{13}C-NMR chemical shifts with available experiments, whereas the ^{1}H-NMR chemical shifts refer to Table S4 in Supplementary Materials.

Table 2. Comparison of the calculated and measured ^{13}C-NMR chemical shifts (δ_C) of exo/endo-THDCPD isomers (ppm).

	Endo-THDCPD			Exo-THDCPD			
 Exo-THDCPD	**B3LYP ^**	**B3PW91 ^**	**Expt [1#]**	**B3LYP ***	**B3PW91 ^**	**Expt [1#]**	**Expt [2#]**
C1	50.49	45.31	45.49	52.92	47.60	48.18	48.28
C2	50.49	45.31	45.49	52.92	47.60	48.18	48.28
C3	46.82	41.89	41.57	44.59	39.95	40.65	40.74
C4	46.82	41.89	41.57	44.59	39.95	40.65	40.74
C5	44.26	40.41	43.28	33.06	29.23	32.07	32.12
C6	25.10	21.14	23.07	30.86	26.69	28.76	28.82
C7	25.10	21.14	23.07	30.86	26.69	28.76	28.82
C8	29.26	25.26	26.98	34.63	30.49	32.42	32.48
C9	29.26	25.26	26.98	34.63	30.49	32.42	32.49
C10	30.15	26.03	28.74	29.53	24.95	27.25	27.29
RMSD [1]	**3.56**	**1.71**	**(5.20) [%]**	**3.17**	**1.76**	**(5.20) [%]**	**-**
RMSD [2]	**-**	**-**	**-**	**3.10**	**1.82**	**-**	**-**

^ With the same aug-cc-pVTZ basis set. * Using build-in δc(TMS) = 182.66 ppm and δ_H(TMS) = 31.88 ppm in chloroform ($CHCl_3$) solvent. # In deuterated chloroform ($CDCl_3$) solvent. * Root mean square deviation (RMSD), RMSD [1] with respect to Exp [1#] [44], and RMSD [2] with respect to Exp [2#] [43]. The latter is only available for exo-THDCPD. Refer to the Supplementary Materials for detailed RMSD calculations. [%] The RMSD of the measured NMR [44] between exo and endo isomers reveals the differences between the exo- and endo- ^{13}C-NMR measurements and, therefore, the differences between the isomer pair.

As shown in Table 2, the DFT B3PW91 functional is slightly more accurate for ^{13}C-NMR than the B3LYP functional, yielding lower RMSD[1] values of 1.71 ppm for endo-THDCPD and 1.76 ppm for exo-THDCPD, in agreement with our early study [11]. The RMSD value between the exo and endo isomers of the measured ^{13}C-NMR is as large as 5.20 ppm, which reveals that the local chemical environments of exo- and endo-isomers are quite

different. For ^{1}H-NMR, DFT B3PW91, and B3LYP, calculations aligned more closely with experimental shifts, though B3LYP showed slightly better accuracy [11], producing the RMSD values of 0.24 ppm for endo-THDCPD and 0.32 ppm for exo-THDCPD, as shown in Table S4 in Supplementary Materials. Notably, discrepancies in the ^{1}H-NMR data for Carbons 8 and 9, reported by Hu et al. [44], suggest potential inaccuracies in their experimental methods or a reporting error, as these values deviate significantly from the more consistent results reported by Bui et al. [43]. These findings indicate that the potential of DFT methods, particularly when appropriately chosen, can enhance the accuracy of NMR predictions and minimize errors in computational and experimental analyses.

Figure 3 displays the ^{13}C-NMR chemical shifts (δ_C) of the isomers. All δ_C's span within 20–50 ppm, indicating all chemical bonds in the isomers are single C-C bonds. The δ_C's of the junction carbons C1/C2 and C3/C4 is located on the higher side of 40 ppm, which is larger than the alkane chemical shift range (10–40) ppm for CH- and CH_2-functional groups [45]. Similarly, ^{1}H chemical shifts (see Table S4 in Supplementary Materials) are also higher than typical alkane values (0.94–1.57 ppm) [27], further underscoring the impact of the strain in the isomers. The ^{13}C-NMR spectra of exo/endo isomers are very different, including shifting and swapping. The δ_c shifts at the triangle tips in the structures, such as the positions of flagpole C5, are large between the isomers. For example, the δ_C of flagpole C5 (red) exhibits a pronounced shift/swap of the isomers, δ_C (C5) of exo-THDCPD is 29.23 ppm whereas, the same C5 in endo-THDCPD is given by 40.41 ppm, a change of over 11.18 ppm.

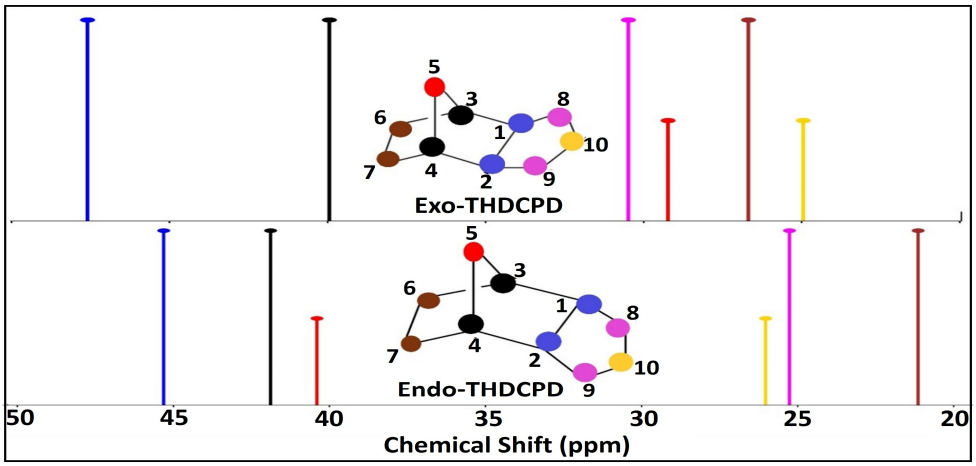

Figure 3. Comparison of ^{13}C-NMR chemical shifts in isomers of endo-/exo-THDCPD isomers calculated using DFT B3PW91/aug-cc-pVTZ model. The largest of the measured chemical shifts in exo- and endo-THDCPD is $\Delta\delta_{C5}$ = 11.16 ppm.

The position of δ_C (C5) changes from the 3rd largest in end-THDCPD to the 3rd smallest in exo-THDCPD, a shift of over 10 ppm ($\Delta\delta$ = 11.18 ppm). This may be caused by the stronger intramolecular interaction of the flagpole C5 and the boat tip C10 in the exo-isomer, the distance between C5···C10 is 3.85 Å, whereas the distance between C5···C10 is given by 4.26 Å for endo-isomer. Interestingly, the boat tip δ_C (C10) exhibits only a small shift but becomes the smallest δ_C (C10) in exo-THDCPD, shifting from the 3rd smallest position after δ_C (C8/C9) and δ_C (C6/C7). This observation suggests that the chemical shift in the flagpole C5 is more sensitive to the boat tip C10. As shown in Figure 3, δ_C (C6/C7) also shifts apparently in endo- and exo-isomers, which are likely caused by the strain contained in the C6-C7 bond-length changes (Δr = 0.03 Å), as indicated in Figure 1.

To explore the larger than usual ^{13}C-NMR chemical shifts in the junction carbons pair of C1/C2 and C3/C4 in the exo-/endo-THDCPD isomers, we calculated Mulliken atomic

charges of the isomers, which are given in Figure 4. It is well known that the Mulliken charges are based on partitioning electron density between atoms in a molecule [46]. Although Mulliken charges depend heavily on the choice of basis set and method, the B3LYP/aug-cc-pVTZ method exhibits sufficient accuracy in calculating NMR chemical shifts in the isomers. Interestingly, although no other atoms have larger electronegativity than carbon atoms in a hydrocarbon compound, the junction carbon atoms exhibit less electron density or are even positively charged. For example, the junction atoms (bridge heads) C3/C4 (dark red) are less negatively charged than other carbon atoms (red) in the isomers, together with the boat tip C10 in the endo-THDCPD isomer, which displays less positive charges (dark red), which is quite different from the boat tip C10 in exo-isomer in the same figure. The rotational axis C1/C2 exhibits positive charges, opposite to all other carbon atoms in the isomers. These carbon atoms with either positive charges (green) or less negative charges (dark red) in the hydrocarbons in Figure 4 reveal that their chemical bonding and geometries can be highly non-standard, such as strain effects and through-space interactions.

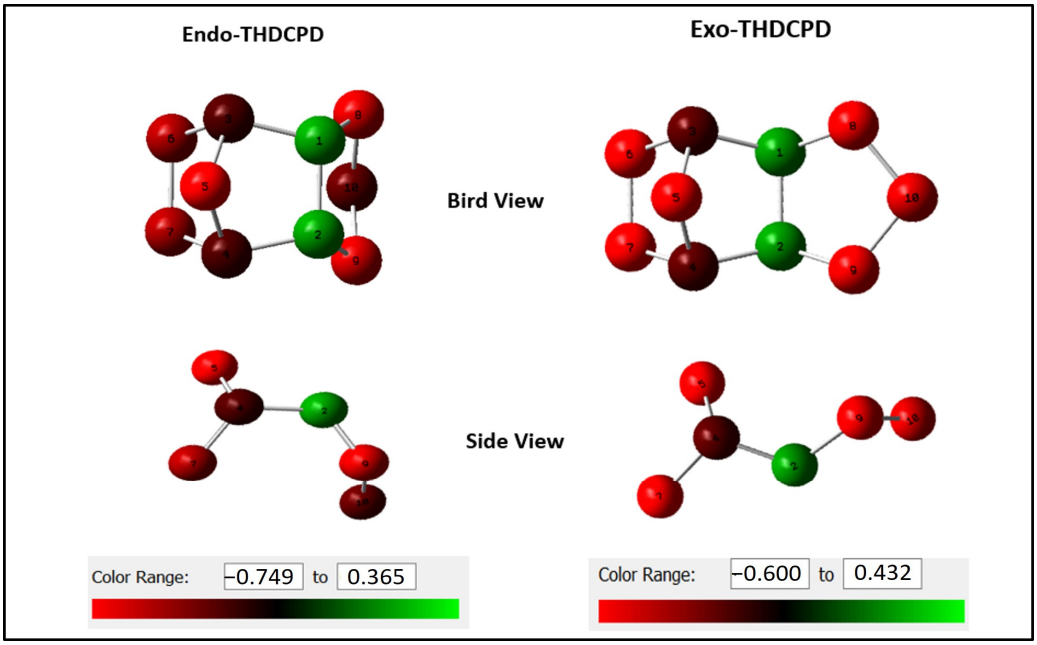

Figure 4. The calculated Mulliken atomic charges of the endo-/exo-THDCPD isomers. Red represents negative charges, and green represents positive charges. Note that all hydrogen atoms, which are all positive (green), are not presented.

3.3. Vibrational Spectra

Vibrational spectroscopy is a valuable tool for investigating molecular structures containing functional groups or unique bonding characteristics [40]. It deciphers molecular vibrations to reveal detailed information about bond types (e.g., C-H, C=C, or strained rings) and assesses chemical concentrations. This technique provides critical insights into structural strain inherent in fuels under study [41,42,46,47]. It is also useful in monitoring thermal stability and decomposition pathways by tracking vibrational frequency shifts under various conditions. Figure 5 compares the calculated IR spectra (FWHM = 4 cm^{-1}) with experimental measurements of Brotton et al. [42] for the exo-isomer. The general agreement between the calculated and measurements is achieved. The IR spectrum of the exo-isomer is more intensive than the endo-isomer, which agrees well with the measurement of Hu et al. [44]. The fully calculated vibrational frequencies of the isomers refer to Table S5 in Supplementary Materials. Due to small dipole moments, the IR spectra of

the hydrocarbon isomers are quite "clean", with the apparent vibrations concentrating on regions of 1500 cm^{-1} and 3000 cm^{-1}, respectively. Further examination of the IR spectra found that the IR band at 1500 cm^{-1} is dominated by CH_2 waving or bending vibrations. In contrast, the band at 3000 cm^{-1} has a concentration of CH_2 and CH stretching vibrations.

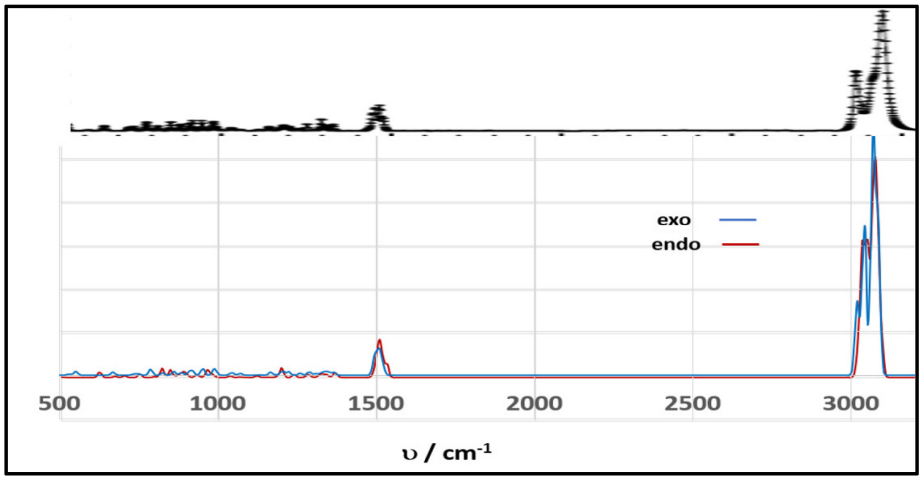

Figure 5. Comparison of calculated IR spectra (red exo-THDCPD, blue endo-THDCPD) with measured IR spectrum of exo-THDCPD from Brotton et al., reproduced with permission from reference [42]. Copyright (2022) American Chemical Society.

The IR band at 3000 cm^{-1} of both isomers is vibrational intensive, and therefore, we target this band. Figure 6 compares the 3000 cm^{-1} band of the IR spectra of the isomers, together with the major band assignments. It is apparent that the variations in the IR spectra between the isomers are due to the strength of CH_2 and C-H stretching vibrations [47], as C-H bonds are stronger than C-C bonds in the hydrocarbons. The six apparent bands in the spectra are labeled as A, B, C, D, E, and F for the exo-isomer, whereas the bands at similar positions are labeled as A′, B′, C′, D′, E′, and F′ for the endo-isomer. Under the same conditions, the most intensive IR vibration in Band D of the exo-isomer at $\upsilon(I_{max})$ = 3070 cm^{-1} with an intensity of D = 150.77 (10^{-40} esu^2 cm^2). Similarly, the corresponding Band D′ for the endo-isomer appears at $\upsilon(I_{max})$ = 3069 cm^{-1} with an intensity of D = 151.17 (10^{-40} esu^2 cm^2). However, the overall IR spectra band intensity of the endo-isomer is less intensive, the ratio is 0.789 of the intensity of the exo-isomer. This is due to the fact that the distribution of the vibrational transitions around the $\upsilon(I_{max})$ of the exo-isomer is more intensive than the endo-isomer, which has been clearly indicated in the IR spectra given in Figure 6.

The spectra in Figure 6 clearly indicate that the IR spectra do not belong to the same molecule. For example, the IR Band F of exo-THDCPD at υ = 3089 cm^{-1} and Band F′ of endo-THDCPD at υ = 3109 cm^{-1}, although close in frequencies, are assigned to different vibrations. As shown in the assignment in the same figure, Band E (υ = 3089 cm^{-1}) of the exo-isomer is dominated by the C(5)-H2 asymmetric stretches, whereas the Band E (υ = 3109 cm^{-1}) of the endo-isomer is assigned to the C(6)-H2, C(7)-H2 and C(10)-H2 asymmetric stretches. The most intensive Band D at $\upsilon(I_{max})$ = 3070 cm^{-1} of the exo-isomer is dominated by the C3-H/C4-H; C6-H(up)/C7-H(up) asymmetric stretches, whereas the most intensive Band D′ at $\upsilon(I_{max})$ = 3069 cm^{-1} of the endo-isomer by vibrations of the C3-H and C4-H asymmetric stretch vibrations. It is interesting that Band C′ at 3050 cm^{-1} of the endo-isomer is a collection of C6-H2/C7-H2, C1-H/C2-H, C8-H2/C9-H2 and C10-H2 symmetric stretches. The close frequency vibration in Band C at 3045 cm^{-1} of the exo-isomer is a collection of symmetric stretches of C5-H2, C6-H2/C7-H2, C3-H/C4-H, and C1-H2/C2-H2, which is the norbornane skeleton. The IR spectra of the exo-/endo-isomer in

Figure 6 clearly demonstrate that the orientation and the shape of the THDCPD compound can affect the molecular geometric and electronic structures and, therefore, spectroscopy.

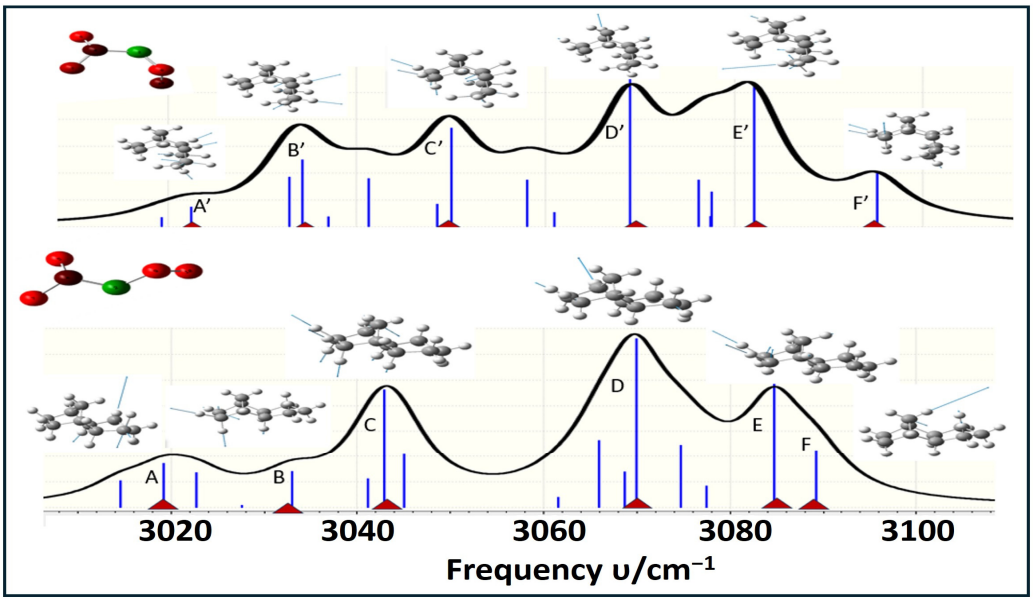

Figure 6. Comparison of calculated IR spectra of exo-THDCPD (**bottom**) and endo-THDCPD (**top**) in the IR region of 3000–3100 cm^{-1}.

3.4. Valence Molecular Orbitals of the Isomers

The ^{13}C-NMR chemical shifts and IR spectroscopy in previous sections have revealed the differences between the exo- and endo-isomers. Here, the valence molecular orbitals of the isomers are further explored for their electronic structural differences. Table 3 compares the calculated electronic properties of the isomers. It is seen that all the properties in Table 3 are without large differences, with discrepancies within the error bars. Many properties in Table 3, however, depend on the wavefunctions (or orbitals), which are usually less sensitive to angular-dependent properties. The energy gap between the highest occupied molecular orbital (HOMO) and the lowest unoccupied molecular orbital (LUMO) [46], $\Delta E = E_{LUMO} - E_{HOMO}$, is given by 7.37 eV and 7.63 eV for the endo-isomer and exo-isomer, respectively, which is even larger than the total electronic energy difference (15.5 kJ/mol) between the isomers. Electronegativity represents the molecule's tendency to attract electrons toward itself when interacting with other molecules or atoms. In strained systems (e.g., bicyclic molecules), electron density distribution can enhance electronegativity in certain areas. The electronegativity of the exo-isomer (−4.14 eV) is more negative than the endo-isomer (−4.05 eV); hence, the exo-isomer has a slightly greater ability to attract and hold electrons.

Table 3. Comparison of electronic properties of the exo-/endo-THDCPD isomers *.

Parameter	Endo-THDCPD	Exo-THDCPD
E_{HOMO} (eV)	−7.73	−7.95
E_{LUMO} (eV)	−0.36	−0.32
$\Delta E_{HOMO-LUMO}$ (eV)	7.37	7.63
Electronegativity (χ) (eV)	−4.05	−4.14
Hardness (η) (eV)	3.69	3.82
Softness (σ) $(eV)^{-1}$	0.27	0.26
Electrophilicity (ψ) (eV)	1.11	1.12

* E_{HOMO} and E_{LUMO} were obtained using the B3LYP/aug-cc-pVTZ method. Refer to the Supplementary Materials for a detailed calculation of electronic properties.

Excess orbital energy spectrum (EOES) [17] highlights the orbital energy differences ($\Delta E = E_{Endo} - E_{Exo}$) of two isomers, offering orbital-based insights into the structural and electronic distinctions between the exo-/endo-isomers. As a result, Figure 7 plots the EOES for the THDCPD isomers using their orbital energies without any orbital symmetry corrections. The discussion will concentrate on the valence orbitals as they experience significant changes in isomerization. The discussion will concentrate on the orbitals with EOES outside of the green box and HOMO, a total of five orbitals pairs. They are orbitals 38a (HOMO), 27a, 20a, 15a and 14a, as shown in Figure 7. As seen in this figure, all valence orbitals of the isomer pair change, as apart from some core orbitals, orbital energies of all valence orbitals of the isomer pair are not the same, indicating that the exo-/endo configurations change the valence electronic structures of the isomers, except for orbital 24a, which can be accidentally equal orbital energy, as the orbital distributions (the insert) of this orbital is very different in the isomers.

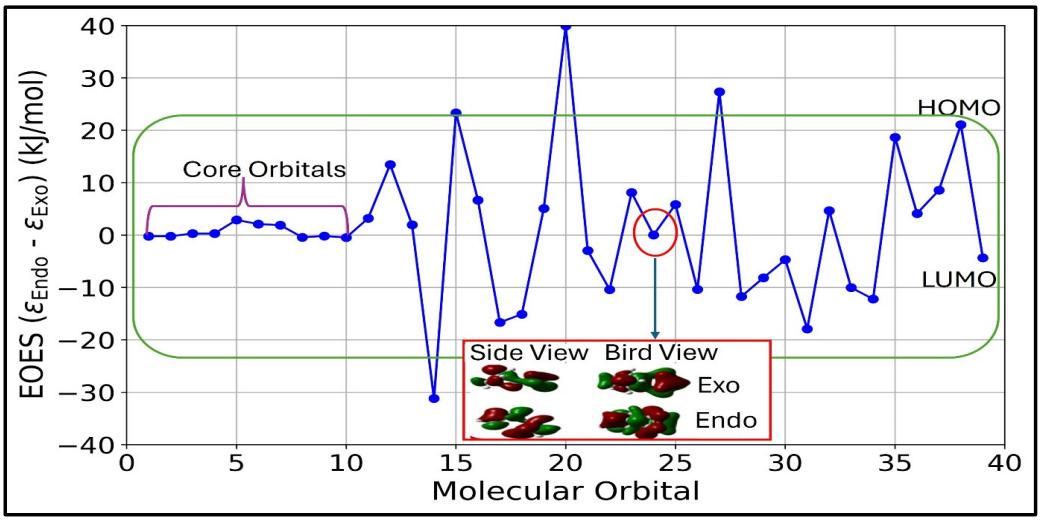

Figure 7. Excess orbital energy spectrum (EOES) of exo-/endo-THDCPD, $\Delta\varepsilon_i = \varepsilon_i(endo) - \varepsilon_i(exo)$, using DFT B3LYP/aug-cc-pVTZ model. Orbital 24a has accidentally had the same energy; their orbital densities differ.

The valence electron distributions of the isomer are quite different, which impacts their physicochemical properties. The EOES also indicates that all valence spaces of the isomers change, including the inner and outer valence spaces. The inner valence orbitals exhibit shifts that alter steric interactions, bond length, and bond angles, as highlighted by previous research [17,48]. Frontier orbitals such as HOMO and LUMO cannot be ignored, although inner valence orbitals demonstrate significant changes. For this reason, Figure 8 reports the HOMO-LUMO energy gap and the electron distributions of HOMO and LUMO of the isomers. As already known from Table 3, the HOMO-LUMO energy gap of the endo-THDCPD isomer is 7.37 eV, which is 0.26 eV for the exo-isomer of 7.63 eV. A larger HOMO-LUMO energy gap typically correlates with stability and lower reactivity, suggesting that exo-THDCPD may be more stable and less reactive under combustion conditions. This stability is particularly beneficial for aviation fuel applications, where thermal resilience is critical for safety and efficiency [49].

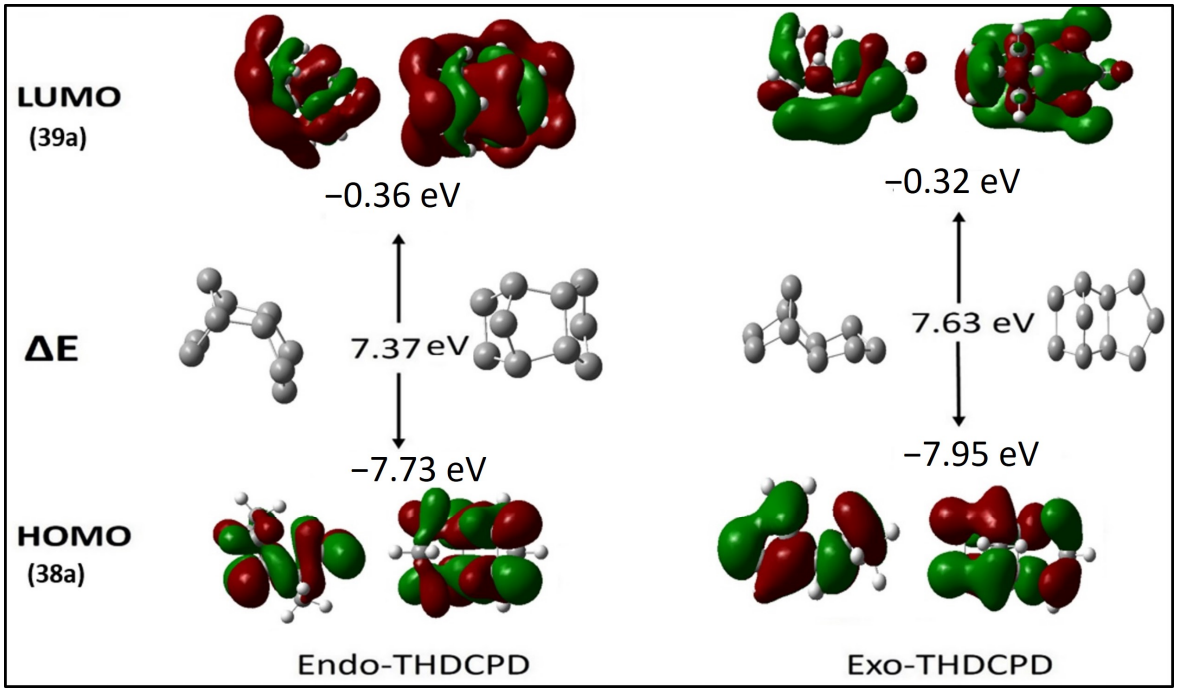

Figure 8. The HOMO and LUMO orbitals of the two isomers of THDCPD and the HOMO-LUMO transitions (side view (**left**) and bird view (**right**)).

The electron densities of the HOMOs (38a) of the isomer exhibit symmetry through the flagpoles C5 and C10, as shown from the bird views. However, the side views of the HOMOs indicated that the HOMO of the exo-isomer is more delocalized so that it has lower orbital energy of −7.95 eV, whereas the same orbital of the endo-isomer with more nodal planes possesses higher orbitals energy of −7.73 eV. The situations in the LUMO orbitals are different. Although the LUMO orbitals of the isomers are different, they share the feature that both LUMOs are largely delocalized. Hence, their orbital energies are closely lying; that is, the LUMO energy of the exo-isomer is −0.31 eV, whereas the endo-isomer is −0.36 eV. Another very interesting feature of the LUMOs of the isomers is that space density overlaps underneath the norbornane skeleton. This through-space density can be inherited from norbornane [21]. The additional triangular structure of ΔC8-C10-C9 distorts the LUMO density but extends to a larger area of delocalization, impacting the electronic structures of the isomers in the future.

Strained molecular structures, such as multi-ring or cage-like hydrocarbons, lead to high internal potential energy [2,5,7]. The strain energy in hydrocarbons arises from deviations in bond angles, torsional angles, and steric interactions relative to ideal conditions in a molecule. These deviations create internal strain, increasing the molecule's energy, which can be released during chemical reactions such as combustion. The major types of strain energies in hydrocarbons include ring strain and bond stretch strain [2,5]. The former is a combination of angle and torsional strain, which occurs when bond angles deviate from the ideal sp^3 hybridization angle of 109.5° [2,5,7], found in cyclic hydrocarbons and the latter happens when bond lengths deviate from ideal values [44]. For instance, quadricyclane (C7H8) exhibits high energy density due to its significant strain energy, despite having fewer hydrogen atoms than other hydrocarbons [3]. Similarly, cyclopropane and cyclobutane demonstrate considerable strain energy due to their pronounced deviations from optimal bond angles [50]. Measuring strain energy empirically, often using cyclohexane as a strain-free reference, highlights the critical role of ring strain in determining hydrocarbons' overall energy content [51]. This understanding is essential for optimizing fuel molecules for high energy density. Besides fuel applications, exo- and endo-THDCPD molecules could

be explored for molecular solar thermal energy storage (MOST), leveraging conformational changes to store and release energy [52]. Additionally, their HED makes them potential candidates for energy-intensive chemical reactions, advanced materials, and photochemical applications. This motivates further research into the applicability of THDCPD in areas such as renewable energy systems and other innovative sectors.

4. Conclusions

This study provides detailed theoretical insights into the structures and properties of the JP-10's fuel exo- and end-isomers. The density functional theory (DFT) calculations reveal that the exo-isomer is more stable (by 15.51 kJ/mol) without the additional through-space interaction in the endo-isomer where the triangular ring (ΔC8-C10-C9) flips from underneath the norbornane skeleton, which introduces additional strain.

The calculated ^{13}C-NMR spectra and vibrational (infrared) spectra, which align well with recent experimental measurements, reveal distinct differences in the carbon chemical environments of the isomers and are consistent with findings from our recent exo-THDCPD chair/boat study. The extra strain in the endo-isomer leads to apparent chemical shifts in the flagpole carbons (C5) and boat tip carons (C10), which engage with fewer positive charges. Moreover, the junction carbons (C1/C2), which control the rotation from exo-isomer to endo-isomer, turn into positively charged, accumulating considerable strain. The calculated infrared (IR) spectra of the isomers, which are validated by experimental results, show distinct vibrations responsible for the signals.

The EOES indicates that while many physical properties of the isomers fall within error bars, the valence electronic structure of the isomers is significantly different. Notably, the exo-isomer's HOMO-LUMO gap (7.63 eV) is larger than that of the endo-isomer (7.37 eV), attributed to the more delocalized HOMO of the exo-isomer (−7.95 eV), compared to the endo-isomer (−7.73 eV). These structural, spectroscopic, and electronic differences underscore the unique fuel properties of exo-THDCPD, making it the preferred form of JP-10 fuel.

Supplementary Materials: The following supporting information can be downloaded at https://www.mdpi.com/article/10.3390/pr13020543/s1. Figure S1: Optimized structure of Ethane using B3LYP/aug-cc-pVTZ model; Figure S2: ^{1}H NMR spectra of endo-THDCPD using B3LYP/aug-cc-pVTZ model; Figure S3: ^{1}H NMR spectra of exo-THDCPD using B3LYP/aug-cc-pVTZ model; Figure S4: Comparison of the calculated IR wavenumbers of exo-THDCPD using B3LYP/aug-cc-pVTZ model with the experiment; Table S1: Cartesian coordinates of exo-THDCPD and endo-THDCPD using B3LYP/aug-cc-pVTZ model; Table S2: Comparison of bond length, angles, and dihedrals of two isomers of THDCPD using B3PW91 and B3LYP functiaonals and aug-cc-pVTZ basis set; Table S3: Comparison of bond length of Ethane with literature; Table S4: Comparisons of ^{1}H-NMR of endo-and exo-THDCPD using B3LYP and B3PW91 functional and aug-cc-pVTZ basis set; Table S5: Comparison of the calculated IR with the experimental values and those computed by Brotton et al. [42]. References [53–55] are cited in the Supplementary Materials.

Author Contributions: Conceptualization, F.W.; writing—original draft, D.R.; methodology, D.R. and F.W.; visualization, D.R. and F.W.; analysis, D.R. and F.W.; writing—review and editing, D.R. and F.W.; project administration, F.W.; review V.V. and Y.Y.; supervision, F.W. and V.V.; partial financial support, Y.Y. All authors have read and agreed to the published version of the manuscript.

Funding: This research was partly supported by scholarships from the Commonwealth Scientific and Industrial Research Organization (CSIRO, Australia) and The Australian Defense Science Institute (DSI), an initiative of the State Government of Victoria.

Data Availability Statement: The original contributions presented in this study are included in the article/Supplementary Materials. Further inquiries can be directed to the corresponding author.

Acknowledgments: D.R. acknowledges the Tuition Fee Scholarship of the Swinburne University of Technology. The authors thank supercomputing facilities provided by Swinburne University of Technology Supercomputing Facilities (OzSTAR and Ngarrgu Tindebeek (which means "Knowledge of the Void" in the Moondani Toombadool language)).

Conflicts of Interest: Author Yunxia Yang was employed by the CSIRO Energy. The remaining authors declare that the research was conducted in the absence of any commercial or financial relationships that could be construed as a potential conflict of interest. The CSIRO Energy had no role in the design of the study; in the collection, analyses, or interpretation of data; in the writing of the manuscript, or in the decision to publish the results.

References

1. Xiao, Z.; Zhang, C.; Huang, S.; Zhang, S.; Tan, X.; Lian, Z.; Zou, J.-J.; Zhang, X.; Li, G.; Wang, D. A comprehensive review on steam reforming of liquid hydrocarbon fuels: Research advances and Prospects. *Fuel* **2024**, *368*, 131596. [CrossRef]
2. Wang, F.; Rijal, D. Sustainable Aviation Fuels for Clean Skies: Exploring the Potential and Perspectives of Strained Hydrocarbons. *Energy Fuels* **2024**, *38*, 4904–4920. [CrossRef]
3. Boehm, R.C.; Yang, Z.; Bell, D.C.; Faulhaber, C.; Mayhew, E.; Bauder, U.; Eckel, G.; Heyne, J.S. Perspective on Fuel Property Blending Rules for Design and Qualification of Aviation Fuels: A Review. *Energy Fuels* **2024**, *38*, 17128–17145. [CrossRef]
4. Kosir, S.; Heyne, J.; Graham, J. A machine learning framework for drop-in volume swell characteristics of sustainable aviation fuel. *Fuel* **2020**, *274*, 117832. [CrossRef]
5. Rijal, D.; Vasilyev, V.; Wang, F. Advancing Sustainable Aviation Fuel Design: Machine Learning for High-Energy-Density Liquid Polycyclic Hydrocarbons. *Energy Fuels* **2025**. [CrossRef]
6. AIRBUS. Available online: https://www.airbus.com/en/newsroom/press-releases/2024-06-worlds-first-in-flight-study-of-commercial-aircraft-using-100 (accessed on 23 October 2024).
7. Chen, S.; Li, J.; Zhu, Q.; Li, Z. Study on the initial pyrolysis kinetics of strained polycyclic hydrocarbons. *Fuel* **2023**, *351*, 128903. [CrossRef]
8. Bruno, T.J.; Huber, M.L.; Laesecke, A.; Lemmon, E.W.; Perkins, R.A. Thermochemical and thermophysical properties of JP-10. *Tech. Rep.* **2006**, *6640*, 325.
9. Chenoweth, K.; Van Duin, A.C.; Dasgupta, S.; Goddard Iii, W.A. Initiation mechanisms and kinetics of pyrolysis and combustion of JP-10 hydrocarbon jet fuel. *J. Phys. Chem. A* **2009**, *113*, 1740–1746. [CrossRef] [PubMed]
10. Schapin, N.; Majewski, M.; Varela-Rial, A.; Arroniz, C.; De Fabritiis, G. Machine learning small molecule properties in drug discovery. *Artif. Intell. Chem.* **2023**, *1*, 100020. [CrossRef]
11. Wang, F.; Vasilyev, V. Unveiling JP-10 Fuel: A DFT and NMR Study of Exo-TCD Chair and Boat Conformers. *ChemRxiv* **2024**. *preprint*. [CrossRef]
12. Wang, F.; Chong, D.P. Polycycloalkanes at the Helm: Exploring high energy density eFuel with norbornyl derivatives. *Mater. Today Chem.* **2024**, *41*, 102264. [CrossRef]
13. Caceres-Martinez, L.E.; Lopez, J.S.; Dagle, R.A.; Gillespie, R.; Kenttämaa, H.I.; Kilaz, G. Influence of blending cycloalkanes on the energy content, density, and viscosity of Jet-A. *Fuel* **2024**, *358*, 129986. [CrossRef]
14. *ASTM D4054-19*; Practice for Qualification and Approval of New Aviation Turbine Fuels and Fuel Additives. ASTM International: West Conshohocken, PA, USA, 2019.
15. *ASTM D7566-22*; Standard Specification for Aviation Turbine Fuel Containing Synthesized Hydrocarbons. ASTM International: West Conshohocken, PA, USA, 2022. [CrossRef]
16. Tong, Y.; Powell, C.B.; Powell, G.L.; Hall, M.B. Theoretical Investigation of Linear Relationships between the Dihedral Torsion Angles and Diosmium Bond Distances in Diosmium Sawhorse Complexes. *Inorg. Chem.* **2024**, *63*, 1898–1908. [CrossRef]
17. Islam, S.; Wang, F. The d-electrons of Fe in ferrocene: The excess orbital energy spectrum (EOES). *RSC Adv.* **2015**, *5*, 11933–11941. [CrossRef]
18. Khan, A.; Chodimella, V.P.; Sharma, A.; Ali, S.S.; Mishra, A.; Anand, M.; Farooqui, S.A.; Kumar, R.; Sinha, A.K. Conversion of dicyclopentadiene into high energy density fuel exo-tetrahydrodicyclopentadiene: An experimental and computational study. *Fuel* **2023**, *334*, 126605. [CrossRef]
19. Zarezin, D.P.; Rudakova, M.A.; Bykov, V.I.; Bermeshev, M.V. Metal chlorides supported on silica as efficient catalysts for selective isomerization of endo-tetrahydrodicyclopentadiene to exo-tetrahydrodicyclopentadiene for JP-10 producing. *Fuel* **2021**, *288*, 119579. [CrossRef]
20. Expanding the Limit of Computation Chemistry. *Gaussian 16*. Available online: https://gaussian.com/gaussian16/ (accessed on 22 October 2024).

21. Jabłoński, M.; Palusiak, M. Basis set and method dependence in atoms in molecules calculations. *J. Phys. Chem. A* **2010**, *114*, 2240–2244. [CrossRef] [PubMed]
22. Reiher, M.; Liégeois, V.; Ruud, K. Basis set and density functional dependence of vibrational Raman optical activity calculations. *J. Phys. Chem. A* **2005**, *109*, 7567–7574. [CrossRef]
23. Porto, C.M.; Nome, R.A.; Morgon, N.H. The influence of basis sets and ansatze building to quantum computing in chemistry. *J. Mol. Model.* **2024**, *30*, 275. [CrossRef] [PubMed]
24. Leal, A.L.; Albuquerque, R.M.; Silva, A.M.; Ribeiro, J.C.; Martins, F.G. Estimation of gasoline properties by 1H NMR spectroscopy with repeated double cross-validated partial least squares models. *J. Chemom.* **2020**, *34*, e3212. [CrossRef]
25. Basu, B.; Kapur, G.; Sarpal, A.; Meusinger, R. A neural network approach to the prediction of cetane number of diesel fuels using nuclear magnetic resonance (NMR) spectroscopy. *Energy Fuels* **2003**, *17*, 1570–1575. [CrossRef]
26. Heredia-Langner, A.; Cort, J.R.; Grubel, K.; O'Hagan, M.J.; Jarman, K.H.; Linehan, J.C.; Albrecht, K.O.; Polikarpov, E.; King, D.L.; Smurthwaite, T.D. Methodology for the development of empirical models relating 13C NMR spectral features to fuel properties. *Energy Fuels* **2020**, *34*, 12556–12572. [CrossRef]
27. Abdul Jameel, A.G. Identification and quantification of hydrocarbon functional groups in gasoline using 1H-NMR spectroscopy for property prediction. *Molecules* **2021**, *26*, 6989. [CrossRef] [PubMed]
28. Ebrahimi, H.P.; Shaghaghi, H.; Tafazzoli, M. Gauge invariant atomic orbital-density functional theory prediction of accurate gas phase 1H and 13C NMR chemical shifts. *Concepts Magn. Reson. Part A* **2011**, *38*, 269–279. [CrossRef]
29. Dennington, R.; Keith, T.A.; Millam, J.M. *GaussView, version 6.0. 16*; Semichem Inc.: Shawnee Mission, KS, USA, 2016.
30. Kim, W.; McMillan, R.A.; Snyder, J.P.; Conticello, V.P. A stereoelectronic effect on turn formation due to proline substitution in elastin-mimetic polypeptides. *J. Am. Chem. Soc.* **2005**, *127*, 18121–18132. [CrossRef] [PubMed]
31. Bu, H.; Zheng, H.; Zhou, H.; Zhang, H.; Yang, Z.; Liu, Z.; Wang, H.; Xu, Q. The role of sp^2 and sp^3 hybridized bonds on the structural, mechanical, and electronic properties in a hard BN framework. *RSC Adv.* **2019**, *9*, 2657–2665. [CrossRef] [PubMed]
32. Pauling, L.; Brockway, L.O. Carbon-carbon bond distances. The electron diffraction investigation of ethane, propane, isobutane, neopentane, cyclopropane, cyclopentane, cyclohexane, allene, ethylene, isobutene, tetramethylethylene, mesitylene, and hexamethylbenzene. Revised values of covalent radii. *J. Am. Chem. Soc.* **1937**, *59*, 1223–1236.
33. Organic Chemistry. Available online: https://www.chemistrysteps.com/bond-lengths-and-bond-strengths/ (accessed on 23 October 2024).
34. Politzer, P.; Murray, J.S. The fundamental nature and role of the electrostatic potential in atoms and molecules. *Theor. Chem. Acc.* **2002**, *108*, 134–142. [CrossRef]
35. van der Wijst, T.; Bickelhaupt, F. Supramolecular switches based on the guanine-cytosine (GC) Watson-Crick pair: Effect of neutral and ionic substituents. *Chemistry* **2006**, *12*, 3032–3042. [CrossRef]
36. Chandler, D.; Weeks, J.D.; Andersen, H.C. Van der Waals picture of liquids, solids, and phase transformations. *Science* **1983**, *220*, 787–794. [CrossRef] [PubMed]
37. Wang, F.; Chatterjee, S. Dominant carbons in trans-and cis-resveratrol isomerization. *J. Phys. Chem. B* **2017**, *121*, 4745–4755. [CrossRef] [PubMed]
38. Zehe, M.J.; Jaffe, R.L. Theoretical calculation of jet fuel thermochemistry. 1. Tetrahydrodicylopentadiene (JP10) thermochemistry using the cbs-qb3 and G3 (MP2)//B3LYP methods. *J. Org. Chem.* **2010**, *75*, 4387–4391. [CrossRef] [PubMed]
39. Boyd, R.H.; Sanwal, S.N.; Shary-Tehrany, S.; McNally, D. Thermochemistry, thermodynamic functions, and molecular structures of some cyclic hydrocarbons. *J. Phys. Chem.* **1971**, *75*, 1264–1271. [CrossRef]
40. Wang, F. Future of computational molecular spectroscopy—From supporting interpretation to leading the innovation. *Phys. Chem. Chem. Phys.* **2023**, *25*, 7090–7105. [CrossRef] [PubMed]
41. Vozka, P.; Kilaz, G. A review of aviation turbine fuel chemical composition-property relations. *Fuel* **2020**, *268*, 117391. [CrossRef]
42. Brotton, S.J.; Perera, S.D.; Misra, A.; Kleimeier, N.F.; Turner, A.M.; Kaiser, R.I.; Palenik, M.; Finn, M.T.; Epshteyn, A.; Sun, B.-J. Combined spectroscopic and computational investigation on the oxidation of exo-tetrahydrodicyclopentadiene (jp-10; c10h16) doped with titanium–aluminum–boron reactive metal nanopowder. *J. Phys. Chem. A* **2021**, *126*, 125–144. [CrossRef]
43. Bui, A.T.; Nguyen, D.L.; Pham, Q.H.; Nguyen, N.H.; Pham, K.D.; Cao, H.T. Optimization of the isomerization reaction of endo-tetrahydrodicyclopentadiene into exo-tetrahydrodicyclopentadiene. *J. Sci. Tech. Sect. Phys. Chem. Eng.* **2024**, *2*. [CrossRef]
44. Yin, H.; Min-chang, W.; Qing, P.; Yan-li, N.; Ying, K.; Ming, W.; Jie-yu, L.; Zhi-qun, C. Spectroscopic Analysis of Endo and Exo-Tetrahydrodicyclopentadiene. *Spectrosc. Spectr. Anal.* **2020**, *40*, 3161–3166.
45. Rakhmatullin, I.Z.; Efimov, S.V.; Klochkov, A.V.; Gnezdilov, O.I.; Varfolomeev, M.A.; Klochkov, V.V. NMR chemical shifts of carbon atoms and characteristic shift ranges in the oil sample. *Pet. Res.* **2022**, *7*, 269–274. [CrossRef]
46. Demircioğlu, Z.; Kaştaş, Ç.A.; Büyükgüngör, O. Theoretical analysis (NBO, NPA, Mulliken Population Method) and molecular orbital studies (hardness, chemical potential, electrophilicity and Fukui function analysis) of (E)-2-((4-hydroxy-2-methylphenylimino) methyl)-3-methoxyphenol. *J. Mol. Struct.* **2015**, *1091*, 183–195. [CrossRef]
47. Coates, J. Interpretation of Infrared Spectra, A Practical Approach. *Encycl. Anal. Chem.* **2000**, *12*, 10815–10837. [CrossRef]

48. Wang, F.; Downton, M. Inner valence shell bonding mechanism of n-butane studied using orbital momentum distributions of its conformational isomers. *J. Phys. B: At. Mol. Opt. Phys.* **2004**, *37*, 557. [CrossRef]
49. Hamilton, J.; Sadat, Y.; Dwyer, M.; Ghali, P.; Khandelwal, B. Thermal stability and impact of alternative fuels. In *Aviation Fuels*; Elsevier: Amsterdam, The Netherlands, 2021; pp. 149–218.
50. Wiberg, K.B. The concept of strain in organic chemistry. *Angew. Chem. Int. Ed. Engl.* **1986**, *25*, 312–322. [CrossRef]
51. Bauzá, A.; Quiñonero, D.; Deyà, P.M.; Frontera, A. Estimating ring strain energies in small carbocycles by means of the Bader's theory of 'atoms-in-molecules'. *Chem. Phys. Lett.* **2012**, *536*, 165–169. [CrossRef]
52. Orrego-Hernández, J.; Dreos, A.; Moth-Poulsen, K. Engineering of norbornadiene/quadricyclane photoswitches for molecular solar thermal energy storage applications. *Acc. Chem. Res.* **2020**, *53*, 1478–1487. [CrossRef] [PubMed]
53. Tamukong, P.K.; Khait, Y.G.; Hoffmann, M.R. Accurate dissociation of chemical bonds using DFT-in-DFT embedding theory with external orbital orthogonality. *J. Phys. Chem. A* **2017**, *121*, 256–264. [CrossRef] [PubMed]
54. Sargsyan, K.; Grauffel, C.; Lim, C. How molecular size impacts RMSD applications in molecular dynamics simulations. *J. Chem. Theory Comput.* **2017**, *13*, 1518–1524. [CrossRef] [PubMed]
55. Azeez, Y.H.; Kareem, R.O.; Qader, A.F.; Omer, R.A.; Ahmed, L.O. Spectroscopic characteristics, stability, reactivity, and corrosion inhibition of AHPE-dop compounds incorporating (B, Fe, Ga, Ti): A DFT investigation. *Next Mater.* **2024**, *3*, 100184. [CrossRef]